Optical Materials EXPRESS

Isotropic contractive scaling of laser written microstructures in vitrified aerogels

NIKOLAOS A. VAINOS,[1,2,*] VAGELIS KAROUTSOS,[1] BEN MILLS,[3] ROBERT W. EASON,[3] AND MICHEL PRASSAS[4]

[1] *Department of Materials Science, University of Patras, Panepistimioupolis, Rion, Patras 26504, Greece*
[2] *Also at the Theoretical and Physical Chemistry Institute, National Hellenic Research Foundation, Athens 16635, Greece*
[3] *Optoelectronics Research Centre, University of Southampton, Highfield, Southampton SO17 1BJ, UK*
[4] *Corning European Technology Centre, 7 bis avenue de Valvins, CS 70156 Samois-sur-Seine, Avon Cedex, 77215 France*
[*] *vainos@upatras.gr*

Abstract: A novel route is presented enabling minimization of feature sizes via laser ablative micro-patterning in highly porous silica aerogel monoliths and subsequent viscous sintering. Vitrification yields isotropically contracted silica solids preserving their original stereometric forms. The contraction depends on aerogel structure and porosity and we demonstrate here the first realization of a 3:1 ratio. Surface relief and void micropatterns inscribed in the monolith also undergo isotropic contraction and feature minimization beyond the spatial resolution of their original recording. Experimental results provide clear evidence that embedded void structures undergo contraction larger than the nominal stereometric scaling. This is a demonstration of a generic principle that enables fundamental physical resolution limits to be surpassed, leading to new avenues in micro- and nano-fabrication technologies.

OCIS codes: (160.4670) Optical materials; (160.2750) Glass and other amorphous materials; (160.1245) Artificially engineered materials; (140.3390) Laser materials processing; (220.4000) Microstructure fabrication; (050.6875) Three-dimensional fabrication.

References and links

1. M. A. Aegerter, N. Leventis, M. M. Koebel, *Aerogels Handbook* (Springer 2011).
2. S. S. Kistler, "Coherent expanded aerogels," J. Phys. Chem. **36**(1), 52–64 (1932).
3. B. J. J. Zelinski and D. R. Uhlmann, "Gel technology in ceramics," J. Phys. Chem. Solids **45**(10), 1069–1090 (1984).
4. L. W. Hrubesh, "Aerogel applications," J. Non-Cryst. Solids **225**, 335–342 (1998).
5. C. G. Brinker and G.W. Scherer, *Sol-gel Science* (Academic 1990).
6. Yu. K. Akimov, "Fields of application of aerogels (Review)," Instrum. Exp. Tech. **46**(3), 287–299 (2003).
7. G. A. Sprehn, L. W. Hrubesh, J. F. Poco, and P. H. Sandler, "Aerogel-clad optical fiber", US patent No 5,684,907 (1997).
8. L. Tong, J. Lou, R. R. Gattass, S. He, X. Chen, L. Liu, and E. Mazur, "Assembly of Silica Nanowires on Silica Aerogels for Microphotonic Devices," Nano Lett. **5**(2), 259–262 (2005).
9. L. Xiao, M. D. W. Grogan, W. J. Wadsworth, R. England, and T. A. Birks, "Stable low-loss optical nanofibres embedded in hydrophobic aerogel," Opt. Express **19**(2), 764–769 (2011).
10. M. D. W. Grogan, S. G. Leon-Saval, R. Williams, R. England, and T. A. Birks, "Optical fibre with an aerogel-filled core," presented at the 2009 Conference Lasers & Electrooptics and 2009 Conference on Quantum Electronics and Laser Science -CLEO/QELS, art. No 5225497, Baltimore 2–4 June, 2009.
11. L. Xiao and T. A. Birks, "Optofluidic microchannels in aerogel," Opt. Lett. **36**(16), 3275–3277 (2011).
12. G. Eris, D. Sanli, Z. Ulker, S. E. Bozbag, A. Jonás, A. Kiraz, and C. Erkey, "Three-dimensional optofluidic waveguides in hydrophobic silica aerogels via supercritical fluid processing," J. Supercrit. Fluids **73**, 28–33 (2013).
13. S. T. Reed, "Method of patterning an aerogel," US patent No 8,226,839 (2012).
14. J. Sun, J. P. Longtin, and P. M. Norris, "Ultrafast laser micromachining of silica aerogels," J. Non-Cryst. Solids **281**(1–3), 39–47 (2001).

#272733 http://dx.doi.org/10.1364/OME.6.003814
Journal © 2016 Received 1 Aug 2016; revised 23 Sep 2016; accepted 24 Sep 2016; published 11 Nov 2016

15. Q. Bian, S. Chen, B.-T. Kim, N. Leventis, H. Lu, Z. Chang, and S. Lei, "Micromachining of polyurea aerogel using femtosecond laser pulses," J. Non-Cryst. Solids **357**(1), 186–193 (2011).
16. B. Yalizay, Y. Morova, Y. Ozbakir, A. Jonas, C. Erkey, A. Kiraz, and S. Akturk, "Optofluidic waveguides written in hydrophobic silica aerogels with a femtosecond laser," Proc. SPIE **9365**, 936518 (2015).
17. V. Karoutsos, D. Alexandropoulos, M. Vasileiadis, N. Leventis, and N. Vainos, "Laser microprocessing of aerogels," presented at the 8th International Conference on Nanosciences & Nanotechnologies, Thessaloniki, Greece, 12–15 July, 2011.
18. E. M. Rabinovich, "Preparation of glass by sintering," J. Mater. Sci. **20**(12), 4259–4297 (1985).
19. J. Frenkel, "Viscous flow of crystalline bodies under the action of surface tension," J. Phys. (USSR) **9**, 385–391 (1945).
20. G. W. Scherer, "Sintering of Low Density Glasses: I. Theory," J. Am. Ceram. Soc. **60**(5–6), 236–239 (1977).
21. T. Woignier, J. Phallippou, and M. Prassas, "Glasses from aerogels Part 1: The synthesis of monolithic silica aerogels," J. Mater. Sci. **25**, 3111–3117 (1990).
22. T. Woignier, J. Phallippou, and M. Prassas, "Glasses from aerogels Part 2: The aerogel-glass transformation," J. Mater. Sci. **25**(7), 3118–3126 (1990).
23. M. Prassas, PhD Thesis, Montpelier, France (1981).
24. J. W. Zarzycki, M. Prassas, and J. E. H. Phalippou, "Preparation of monolithic silica aerogels, the aerogels thus obtained and their use for the preparation of silica glass articles and of heat-insulating materials," Patent FR8111089, US4,432,956.
25. N. A. Vainos, *Laser Growth and Processing of Photonic Structures* (Woodhead 2012)
26. Materials kindly provided by associates I. Michalou(di)s (HT aerogels), Th. Ioannidis and N. Leventis (LT aerogels) or obtained commercially from Aerogel Technologies Inc.
27. J. A. Grant-Jacob, B. Mills, and R. W. Eason, "Parametric study of the rapid fabrication of glass nanofoam via femtosecond laser irradiation," J. Phys. D Appl. Phys. **47**(5), 055105 (2014).
28. A. Emmerling, J. Gross, R. Gerlach, R. Goswin, G. Reichenauer, J. Fricke, and H.-G. Haubold, "Isothermal sintering of SiO_2-aerogels," J. Non-Crystal. Solids **125**, 230–243 (1990).
29. G. W. Scherer, C. J. Brinker, and E. P. Roth, "Sol - gel - glass: III. viscous sintering," J. Non-Cryst. Solids **72**(2-3), 369–389 (1985).
30. A. Emmerling, W. Lenhard, J. Fricke, and G. A. L. Van De Vorst, "Densification Behaviour of Silica Aerogels upon Isothermal Sintering," J. Sol-Gel. Sci. Tech. (Paris) **8**(1–3), 837–842 (1997).
31. G. W. Scherer, S. Calas, and R. Sempéré, "Sintering Aerogels," J. Sol-Gel. Sci. Tech. (Paris) **13**(1–3), 937–943 (1999).

1. Introduction

Hypercritical drying of gels leads to formation of nanoporous aerogel solids exhibiting unique physical and chemical properties that make these materials excellent candidates for numerous applications [1]. Original developments were pioneered by Kistler, producing his, so called, "aerogel" materials, through dehydration of oxide, cellulose and gelatin water-based gels [2]. Numerous novel approaches [3] expanded the field, using silicates, various oxide and non-oxide inorganic, organic and hybrid compositions, as well as pure carbon, opening up a flourishing field of research and numerous diverse applications with significant commercial impact [4].

Major advents in this area are attributed to the versatility of sol-gel processing, which enables the realization of complex compositions and respective tuning of material's physical and chemical properties [5]. Aerogels consist of a glassy skeletal framework formed typically by ~2 nm to 5 nm interconnected particles. It has an extremely high but controlled porosity approaching 99%, usually having pores of ~20 nm on average with a narrow size distribution. The individual structure depends on the aerogel formation, which tailors the specific physical and chemical properties. Materials are typically characterized by their extremely low density silica, as low as $\rho \sim 0.01$ g cm^{-3}, huge specific surface area, $\sigma \sim 1000$ m^2 g^{-1}, very low thermal conductivity, $\kappa \sim 0.02$ W m^{-1} K^{-1} and low values of sound velocity, $\upsilon \sim 100$ m s^{-1}. Transparent members of this family exhibit a refractive index close to air, n ~1.0-1.02, while they may be translucent, colored and / or fluorescent, depending on their chemical composition and structure. Among the major applications emerging in the industrial, construction, energy, aerospace and biomedical sectors, uses in microelectronics and photonics gain an increasing interest, concerning Cerenkov radiation detectors first, and proceeding to electronics and MEMS, to fluorescent light sources and many others [6].

In photonics, the near unity refractive index of these materials reveals a potential for innovative devices and respective applications. Silica and other oxide aerogels have been proposed as optical waveguide and optical fiber cladding materials [7]. The resulting high dielectric contrast enables efficient guiding in nanowires [8] and nanofibers [9], while aerogel filling of photonic crystal fibers amends the operational characteristics [10]. Hydrophobic aerogels incorporating microchannels have been proposed for optofluidic applications [11, 12]. However, owing to aerogel fragility, processing requires specific methods, such as, for example, special lithographic protocols for planar aerogel coatings [13]. Laser processing was demonstrated by using Ti-sapphire femtosecond laser pulses in silica [14] and polyurea aerogels [15], and it was also very recently applied in the fabrication of optofluidics [16]. High precision laser microprocessing with absence of thermal effects has also been demonstrated by the authors, using deep ultraviolet ArF excimer laser pulses at 193 nm [17].

Even though glass ceramics by powder sintering are produced since the ‘40s, the versatility of sol-gel chemistry combined with the sintering of aerogel solids represents a major advance [18]. The role of viscous flow in thermal sintering and densification was first demonstrated by Frenkel [19] and further investigated by Scherer [20]. The high homogeneity, the composition and porosity tuning of aerogels with the relatively low temperature and environmentally friendly processing, constitute significant advantages over traditional melt techniques. A major relevant milestone, concerns the production of high quality pure silica aerogel monoliths [21] suitable for low temperature glass transformation [22]. This novel scheme introduced by Prassas and associates [23, 24] enables high quality silica object forming at relatively low temperature (~1100 °C) as compared to melting methods. Owing to the resulting materials purity and the potential for metal ion (e.g. rare earth) doping, this approach is particularly suitable for photonic applications.

In this work we demonstrate, for the first time to our knowledge, a novel approach for achieving size reduction of microstructures beyond the original pattern fabrication limits. According to our method, a microstructure is laser-written [25] in a highly nanoporous solid object, in our example a silica aerogel monolith. This aerogel solid incorporating the microstructure is subsequently processed, according to specific thermal protocols, and condenses, forming a vitreous silica solid object reduced in size. The contraction ratio depends on the initial aerogel porosity, the specific materials nature and processing parameters. The whole contraction process is spatially linear and isotropic in nature. The resulting object is a dense silica solid having identical stereometric form and incorporating the original microstructures that also become isotropically scaled down. This is a rather generic new approach that is inherently capable for three-dimensional micro- and prospectively nano-fabrication. It surpasses the fundamental physical resolution limitations of the available micro/nanofabrication technologies, such as, for example, the laser or lithographic patterning limited by diffraction to ~λ/2 feature size, and steps beyond the current state-of-the-art.

2. Laser microstructuring of aerogel monoliths

Aerogel monoliths fabricated by high temperature (HT) and low temperature (LT) supercritical drying were used in this work [26]. Both methods provide crack-free solids with practically zero shrinkage. HT monoliths had density in the range of 0.05-0.20 g cm^{-3} and high optical transparency. LT CO_2 supercritically dried monoliths had density in the same range but a lower optical transparency. Infrared spectroscopy revealed the existence of a considerable -OH content, which presented problems in the vitrification stages as outlined in the following sections.

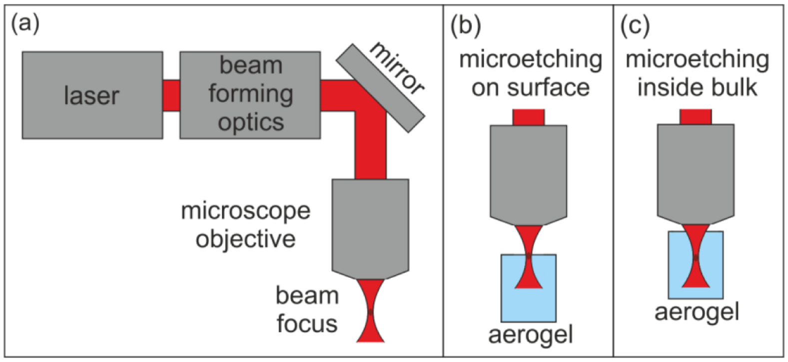

Fig. 1. Schematic of experimental laser processing station (a) including laser source, beam forming optics and focusing or imaging optics. The aerogel monolith was positioned on high precision motion-controlled platforms and processed in two schemes: surface (b) and inside the bulk microetching (c).

Two laser processing facilities (I and II) have been used to perform direct ablative processing of the aerogel monoliths. Both surface relief and three-dimensional void pattering have been implemented and parametrically investigated. Figure 1 presents a schematic of the typical experimental station comprising a laser source, beam shaping and intensity control optics, followed by a beam focusing train with objective optics, as well as sample visualization. The x-y-z motion of the target was facilitated by high precision positioning stages, fully computer automated and linked to laser trigger control. Direct laser ablative processing of the target aerogel sample was achieved by focusing the shaped beam or by projecting an aperture pattern, either on the surface, or inside the bulk material, as outlined in Fig. 1.

Facility I established at the Department of Materials Science, University of Patras, utilizes an ArF excimer laser emitting 8 mJ, 5 ns duration, laser pulses at λ_1 = 193 nm. Maximum repetition rate is at 300Hz, though in most cases irradiation was performed at <100Hz to ensure laser performance stability. By using a range of circular apertures (down to 10μm diameter) the light was projected on the aerogel target by diffraction-limited imaging configuration operating at 17 × demagnification, using an optical system incorporating a 15 × LMU-193 objective, infinity corrected for λ_1 = 193 nm. High fluence values, of the order of ~50 J/cm^2 on target at maximum, can be attained using a fully open circular iris aperture, while intensity was controlled by a dielectric beam-attenuator/compensator pair. The system incorporates x-y-z piezoelectric motion control for sample positioning over a 25 mm × 25 mm area with 80 nm positioning accuracy. z-axis positioning is also controlled using an identical piezo-motorized stage, though the objective's working distance limits its travel range.

The second Facility II, is established at the ORC-University of Southampton, incorporating a Ti:Al_2O_3 femtosecond laser source emitting 4 μJ, 150 fs, laser pulses at λ_2 = 800 nm. The 1 Watt / 250 kHz repetition rate system was also available and used. The system is equipped with pulse extractor and allowed controlled single- and multi-pulse operation. In our work we used a 50 × Nikon CFI60 TU Plan Epi ELWD infinity-corrected objective, focusing micron sized Gaussian laser spots of ~1 J cm^{-2} fluence on target, capable of achieving submicron pattering in focal plane processing. Motion control along the x-y-z directions was achieved by x-y-z motion over a 200 × 50 × 50 mm3 volume by means of computer-controlled motorized stages achieving 250 nm positioning accuracy.

Depending on materials nature, both systems are capable of micron to submicron level direct laser ablative processing of solids based on rather complex physical processes [25]. In the present work, surface patterns and three-dimensional void structures are etched in various silica aerogel monoliths. When applying λ_1 = 193 nm radiation, the energetic 6.42 eV photons are highly absorbed and directly photo-dissociate the skeletal network of the aerogel, with in practice absent thermal effects. To contrast, we note that due to the extremely small thermal conductivity of the aerogel, thermal energy localization is maintained yielding a rapid heat buildup. According to our carbon dioxide laser (λ = 10.6 μm) processing studies, the pure thermal process usually leads to uncontrolled fracture of the material. In the case of femtosecond laser irradiation at λ_2 = 800 nm, wavelength at which the material is fully transparent, the ablation process evolves in a shorter timescale driven by multi-photon absorption and direct ionization, although avalanche ionization may also be initiated secondarily. When focused femtosecond laser beams are used, the multi-photon ablation threshold may be exceeded only within a limited central area in which intensity is appropriately high. A focused beam spot region of dimensions smaller than the nominal Gaussian beam waist is thus effectively used. The peak intensity attained in this region is thus used to ablate features well below the diffraction limited spot size, to even less than 100 nm. It is worth mentioning here that, due to the porous nature of the aerogel, radiation scattering effects can reduce the intensity of the transmitted radiation. Such effects, however, did not seem to cause considerable problems in the overall patterning process.

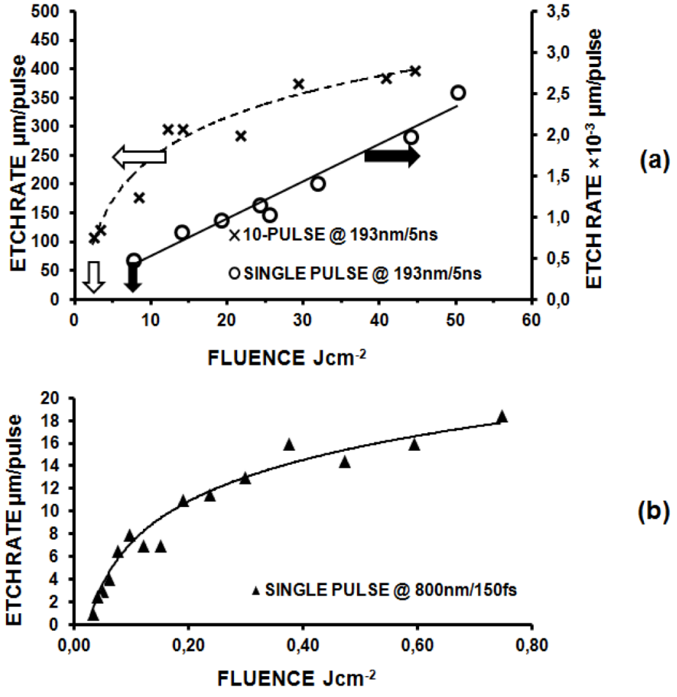

Fig. 2. (a) Etch rate for λ_1 = 193 nm, 5 ns, focused laser beam forsingle pulse(O) and 10 pulse train (×) irradiation at 50 Hz repetition rate.(b) Etch rate for λ_2 = 800 nm, 150 fs, focused laser beam for single pulse irradiation. Ablation threshold fluence values indicated by arrows.

Figure 2 presents results of the study of ablation characteristics of silica aerogel with respect of energy density (fluence) on target for the above cases, using λ_1 = 193 nm and λ_2 = 800 nm. In Fig. 2(a) the ablative etch rate per pulse for the ArF laser λ_1 = 193 nm 5 ns laser pulses is presented for single pulse, solid line (O), and multi-pulse, dashed curve (×), experiments, the latter using a train of 10 pulses at 50 Hz repetition rate. In these experiments a fully open “object aperture” was used yielding an ablated crater of 100 μm in diameter, in order to project an unambiguously defined pattern on target and facilitate accurate energy monitoring by the calibrated NOVA OPHIR bolometer used. Fresnel reflections are negligible owing to the near unity refractive index of the aerogel (n~1). The ablated crater depth considerably exceeds the depth of focus of the laser beam. Fluence on target is controlled in the range of ~10 mJ cm^{-2} to ~50 J cm^{-2}. Peak intensity levels in these experiments are thus estimated in the GW cm^{-2} range, while the use of very small (10s μm) diameter apertures yield considerably lower fluence and intensity levels. Etching values obtained here account for the heavily reduced density of the material, effectively yielding very low absorption figures. Some additional loss caused by radiation scattering may though be expected. On the other hand, the strength of the material is also reduced, thus resulting overall in a rather complex response. The threshold for single pulse ablation at 193 nm is experimentally found close to ~7 J cm^{-2} and it is just below the starting processing point of the solid line in Fig. 2(a). A quite high etch rate (depth μm/pulse) is recorded as a function of fluence and the etching behavior observed falls in the linear regime, far from saturation. Another significant parameter relating to process efficiency is the characteristic specific etching rate, defined as etch-depth - per unit energy density - per laser pulse [25]. At the initial stages it was recorded at 50 μm/[J cm^{-2}]/pulse, remaining at such levels throughout the laser fluence range. In the multi-pulse experiments ablation threshold was found at ~2 J cm^{-2} and the initial specific etching rate was estimated at ~11μm/[J cm^{-2}]/pulse. At the low energy regime, a relatively low threshold value may be expected owing to the accumulated fatigue of the skeletal network caused by the repetitive pulsed irradiation. In contrast, the rather small specific etching rate of ~1.5 μm/[J cm^{-2}]/pulse observed at the high energy end, saturation region of the dashed line in Fig. 2(a), may be justified by the large single-pulse ablation depth achieved by the first pulse(s), while subsequent pulses focused in an already created void produce a reduced net etching effect. This behavior is clearly reflected on the a high specific etching rate of ~60 μm/[J cm^{-2}]/pulse on the high fluence end, characterized by the lack of etch rate saturation for single pulse operation. This is contrasted to the saturated behavior of a low ~1.5 μm/[J cm^{-2}]/pulse specific etching rate recorded for multipulse processing. We note that in our experiments performed using dense fused silica, the multipulse ablation threshold is found at ~0.5 J cm^{-2} while respective ablation rate figures start in the linear regime from ~2 μm/pulse at ~1 J cm^{-2}, saturating to the value of ~3 μm/pulse at fluence values above ~3 J cm^{-2}. In Fig. 2(b) Ti:sapphire femtosecond laser processing at λ_2 = 800 nm is presented. Intensity levels are at the TW cm^{-2} levels. The beam spot size is 6.3μm and single pulse ablation threshold is found to be quite low at 0.02 J cm^{-2}, with a linear specific etch rate of ~80 μm/[J cm^{-2}]/pulse and a terminal value of 24 μm/[J cm^{-2}]/pulse. To contrast, single pulse etching of fused silica is not possible at 800 nm at such fluence levels and multi-pulse processing is required which under certain condition yields nano-foam formation at the surface [27].

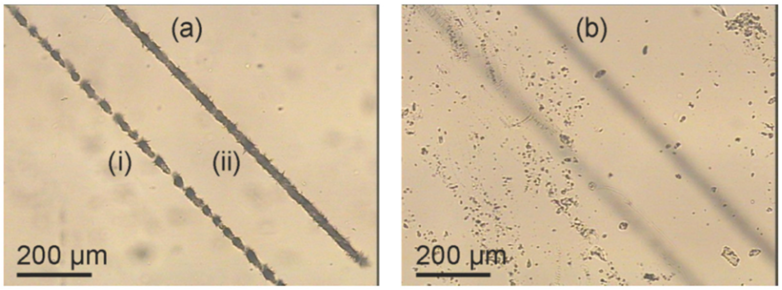

Fig. 3. An example of subsurface patterning (voids (i) and (ii)) by ArF excimer laser radiation at λ_1 = 193nm. Optical microscope images focus (a) inside the bulk and (b) on the flat surface of the aerogel monolith.

Figure 3 presents an example of subsurface processing. Patterns written at ~700 μm below the sample surface are etched using λ_1 = 193 nm laser pulses at rep. rates of 10 Hz (line (i)) and 100 Hz (line (ii)) and 17 × demagnification projection factor. The irradiated aerogel sample was translated at a speed of ~500 μm s^{-1} ablating a series of ~20 μm size voids that are discretely positioned, as in Fig. 3(a)(i), or overlapping to form a linear void channel, as in Fig. 3(a)(ii). The unaffected surface of the aerogel above the processed region is shown in Fig. 3(b), also depicting the out-of-focus channels to illustrate the process. A 10 × / NA = 0.23 imaging objective is used for these observations.

Even though cylindrical monoliths have been used in these experiments, refraction effects are negligible due to the low refractive index of the aerogel, n~1, and thus, high quality processing has also been performed through surfaces of arbitrary stereometry. Nevertheless, scattering may be evidenced in some cases owing to micro-cracks, micro-voids and humidity induced opalescence.

3. Aerogel sintering and microstructure isotropic reduction

Thermal sintering of aerogel bulk leads to a fully dense silica glass that is practically identical to fused silica. This very complex system has been studied extensively by applying a wide range of methodologies [22–24, 28]. This process has also been followed here, evolving in several process stages and comprising a series of distinct and interlaced phenomena that develop under constant heating conditions. It commences from extraction of adsorbed water at temperatures up to ~250 °C, and proceeds to oxidation of organics for up to 500 °C. Dehydration by removal of the water produced in structural OH condensation reactions follows and finally sintering by viscous flow in the range of 1100 °C to 1250 °C, where rapid shrinkage and densification of the material occurs [22]. The formation of siloxane bonds strengthens the aerogel by increasing network connectivity. Subsequently, viscous flow collapses the skeletal network and yields a glassy silica solid having density and physical properties very close, if not identical, to the fused silica produced from the melt. The Frenkel model of nanospheres [19] has a proven validity only for the initial stages of the thermal process. The more generic Scherer approach, considering a skeleton formed by a cubic array of cylinders [20, 29], yields an experimentally verifiable contraction ratio, $c = l/l_o = (\rho_o/\rho)^{1/3}$, where l_o, and l are the linear dimensions and ρ_o, and ρ is the density of the aerogel and the final silica solid, respectively.

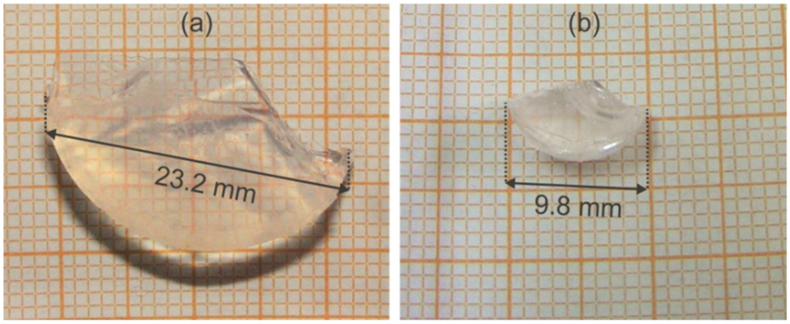

Fig. 4. Aerogel sample having arbitrary stereometric form (a) before and (b) after sintering.

In this work we have applied thermal sintering methods according to Refs. [22-24] comprising slow ramps through thermal process stages at 250 °C, 500 °C, and finally 1100 °C. Densification leads to isotropic contraction even for solids having an arbitrary stereometry, such as that of the broken monolith presented in Fig. 4(a). The isotropically contracted monolith of Fig. 4(b) is smaller by factor of ~ × 2.4, close to the result predicted by the above relation for the relatively dense, ρ ~0.12 g cm^{-3} aerogel sample used. That increased density is also evidenced by the observable refraction effects in Fig. 4(a).

Figure 5 presents the contraction of a void that was laser etched using λ_1 = 193 nm pulses. The void has a diameter of ~84 μm and it is positioned at ~1.5 mm below the surface as shown in Fig. 5(a). After thermal processing, stereometric contraction of the particular aerogel monolith at ratio ~3:1 is attained. The sintered glassy object of Fig. 5(b) incorporates the original void positioned at ~500 μm below the solid surface at the respectively transformed coordinates. This is also denoted by the large out-of-focus defect present on the left of the etched void. The void is photographed through the dense silica surface and image analysis provides a measurement for its lateral size being ~30 μm, meaning a contraction ratio of ~2.8:1, comparable to the stereometric value. We note here the uncertainty of size estimation due to image focus point, while some overestimation of the size of the void after sintering is also anticipated due to imaging through the dense silica, depending on the position of the void.

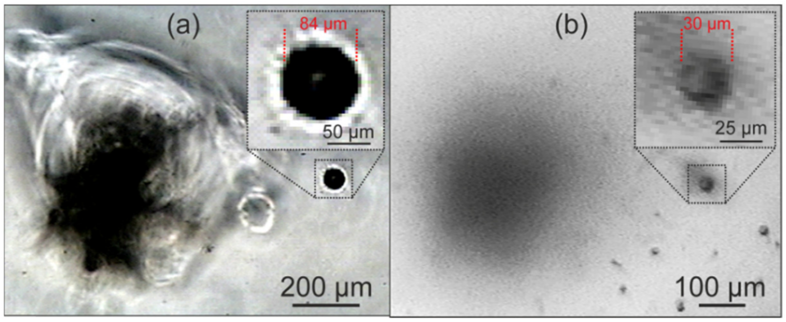

Fig. 5. (a) ArF excimer laser etched void situated at ~1500 μm below the surface. (b) The same void after sintering and contraction of the monolith situated at ~500 μm below the surface as photographed through the glass.

In the above context, contraction by sintering becomes a powerful mechanism for reducing the dimensions of microstructures beyond the limits of the available patterning technology. The sintering protocol has been applied successfully in various unprocessed and laser-processed monoliths. We may note here that a high hydroxyl and/or impurity content in the monolith causes problems in obtaining vitreous silica upon aerogel sintering. The competing crystallization route leads to cristobalite crystalline opals reported before [22], which were also observed and studied in this work, aiming to optimize the thermal processing of low-temperature produced aerogels.

Figure 6 (a) presents a linear periodic surface relief pattern etched on the planar surface of an aerogel monolith using Ti-Sapphire fs laser pulses at λ_2 = 800 nm. The lines have ~8.1 μm width and were etched with a period of ~51.4 μm. The monolith underwent thermal processing according to the protocol. Figure 6(b) presents a micrograph of the planar surface having undergone isotropic contraction that resulted in a linear pattern of ~17.2 μm period. We note that experimental difficulties did not allow reliable and accurate depth profiling, but optical microscopy measurements gave an estimate of feature depth at ~3-5 μm for the original surface and ~0.5-1.0 μm for the sintered surface. However, of clear interest is the shrinkage factor as compared to that of the solid object holding the contracted individual micro-features, the latter being considerably harder to measure. Inhomogeneity of individual structures presented imaging difficulties and thus statistical pixel analysis has been applied to obtain a quantitative shrinkage term. Image analysis software used determines the width of the line at 500 points on the image. By assuming that the boundary of the line occurs at the 50% color intensity threshold (the FWHM), we can accurately obtain size scales, despite the pixelated nature of the zoomed in images. The inset in each image shows a schematic of the automated fitting process. The line width values in the figure correspond to the measured (mean ± standard deviation) and indicate for the original pattern a line-with of (8.1 ± 1.5) μm and for the contracted pattern a line-width of (1.9 ± 0.6) μm. By combining error factors the shrinkage factor for the lines is determined at 4.2 (± 1.5) to one ratio. Note that whilst the 50% threshold value is arbitrary, this value is internally consistent across the two images, and so it provides an accurate shrinkage factor. Size uncertainty is caused by surface defects and the mechanical instability of the system during laser writing. We note that while the line period has been decreased at a ratio ~3:1 in agreement with the stereometric reduction, the structured line-width underwent a ~4.2:1 contraction according to image analysis results, meaning a by 40% larger contraction than the nominal value.

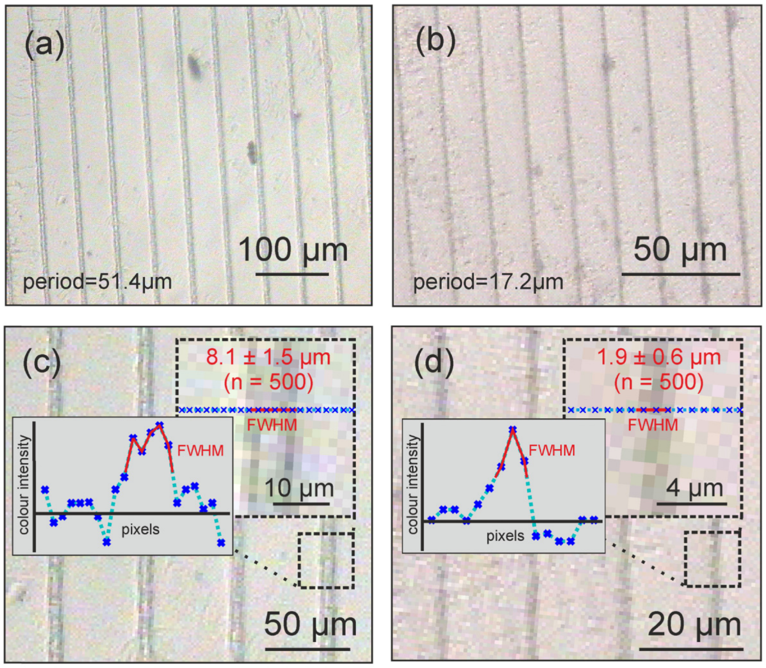

Fig. 6. Contractive scaling of linear surface relief pattern. (a) Original planar aerogel monolith surface laser-patterned at a period of 51.4μm. (b) Planar surface of the sintered silica monolith, comprising the reduced surface relief pattern of period 17.2 μm. Image analysis using 500 independent image points provides an estimate for the width of (c) the original etched surface relief line at (8.1 ± 1.5) μm and (d) the contracted surface relief line at (1.9 ± 0.6) μm.

In the final part of this work the possibility of scaling internally embedded microstructures has been studied and demonstrated. Such an approach is of extreme importance since it allows the production of 3-dimensional structures with impact in a variety of fields. To facilitate the operation, microstructures were laser-written and stably embedded in the aerogel bulk. Figure 7 presents the operation of minimization of such structures patterned directly by laser ablation at various depths inside the aerogel monolith, using the Ti-sapphire fs laser system (λ_2 = 800 nm). In the particular example discussed, a meander pattern was etched at ~3 mm below the planar surface of a cylindrical monolith. Figure 7(a) depicts a detail of the meander structure before sintering as imaged through the aerogel. The pattern has a period of ~101 μm and line width of ~10-15 μm. Pattering accuracy is here affected by the mechanical stability of the aerogel during ablative recording, manifested as line broadening and curling apparent in Fig. 7(a). Upon viscous sintering of the aerogel, isotropic contraction of the solid at ~3.4:1 ratio also results in isotropic minimization of the embedded microstructures. A detail of the contracted structure is optically imaged through this dense vitreous silica and presented in Fig. 7(b). It is located at ~1 mm below the surface and has a period of ~34 μm and a line width of ~4-5 μm. A far view of the planar surface of the sintered silica sample is depicted in Fig. 7(c), bearing major and minor surface defects. In Fig. 7(d), the embedded meander microstructure is imaged by focusing at ~1mm below the silica surface and thus surface defects are imaged out of focus, as expected.

By examining the contraction ratio of the tunnel voids, it appears to have followed the nominal stereometric value of ~3:1. It should be noted, however, that refraction effects add a further uncertainty to the measurements when imaging through the glass. To investigate further the process, we fragmented this particular silica glass sample into smaller pieces. Fragments of the sample comprising cross-sectional surfaces were analyzed experimentally by BET porosimetry resulting in a specific surface area value of 0.63 m^2 g^{-1}, which practically corresponds to "zero" porosity. This result demonstrates the perfect aerogel-to-silica glass transformation throughout the bulk volume.

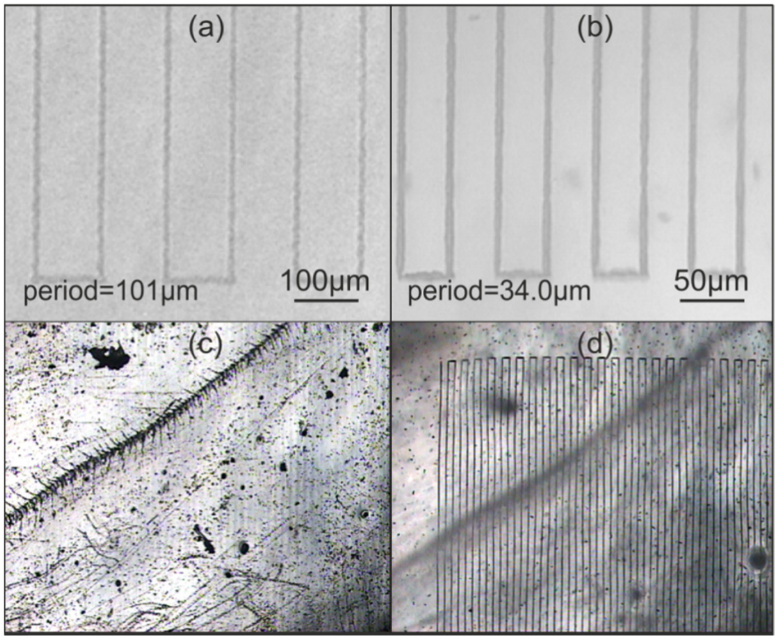

Fig. 7. Isotropic contractive scaling of internally embedded void microstructures. (a) Before processing: detail of laser etched meander microstructure embedded in the aerogel bulk at ~3 mm below the top planar surface; (b) After processing: detail of contracted meander pattern found at ~1mm below the planar surface of the dense silica monolith; (c) Image focus on the top planar surface of sintered monolith isotropically scaled at ratio 3.4:1; (d) part of meander microstructure embedded in the sintered monolith. Image focus is at ~1mm below the top surface. Note the surface defects photographed in-focus (c) and out-of-focus (d).

Figure 8 outlines a further microscopic analysis of exemplar voids embedded in the fractured vitrified sample. Figure 8(a) presents a schematic of the laser path writing a linear meander inside the aerogel bulk monolith. After sintering and contraction, the vitreous sample is sliced as depicted in Fig. 8(b) and thus the tunnel entrances are revealed. A series of void cross sections is presented in the scanning electron micrograph of Fig. 8(c), viewed perpendicular to the fracture surface. We should underline that the internal material structure of the sintered monolith in the fractured region verifies the perfectly solid nature of the vitrified material and provides a definite account for the viscous sintering in the void areas. Figure 8(d) depicts a close up view of the "tunnel entrance" of the particular void indicated. The sample is here highly tilted to provide perspective. All voids appear to have a cylindrical central tubular form with an infrastructural region formed by a complex network of beams of viscously sintered fused silica. This whole is sized in the range of ~5μm, and it is probably caused by the non-uniformity of aerogel patterning due to mechanical instabilities. The very important result is evidenced, however, in the zoomed inset of Fig. 8(d), in which the void "tunnel" clear diameter measures in the range of ~1-2 μm, as shown. Considering that the original pattern is verified to be of the order of ~10-15 μm, there is clear evidence that the contraction ratio exceeds the nominal stereometric value, being in the particular sample ~3.4:1, whereas by ignoring the instability of recording the actual contraction ratio can potentially double or more this nominal value.

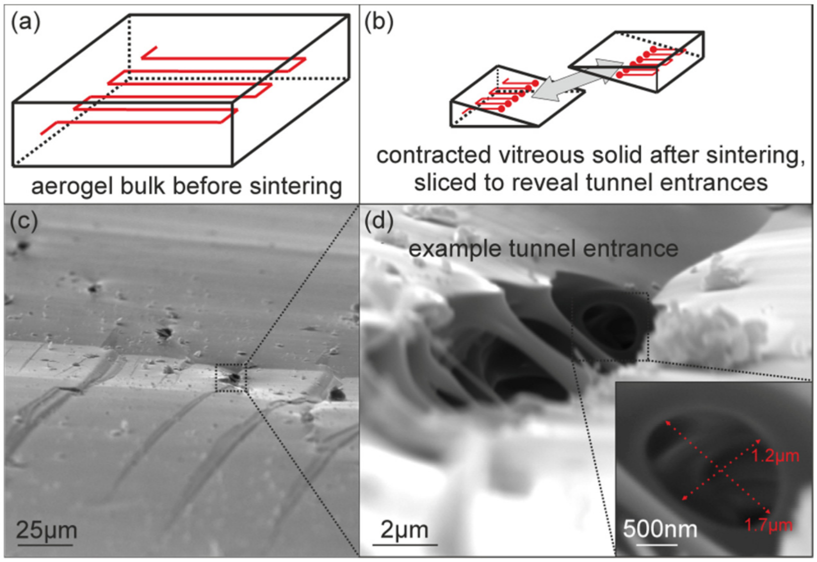

Fig. 8. Microscopic analysis of void microstructures embedded in vitrified aerogel. (a) Laser-patterning path in the unprocessed aerogel monolith; (b) Slicing the contracted vitreous solid reveals the abrupt tunnel entrances of the linear voids; (c) Scanning electron micrograph of a series of tunnel entrances viewed perpendicular to the fractured surface and (d) perspective view of the specific example, indicating zoomed area (inset) of the micron size void entrance.

Such a result is in line with our present observation of increased contraction for the surface relief patterns. In addition, the result agrees quite well with previous comparative analyses concerning densification of macroporous and nanoporous regions during viscous flow, which showed the existence of a higher rate of macropore collapse and preferential aerogel densification [30]. This latter result was backed by theoretical studies on the kinetics of viscous sintering, concluding that such a behavior is theoretically predicted under certain conditions [31]. We may comment here that this technologically advantageous densification behavior would be corroborated by the high surface energy accumulated in the internal surface of the void which is loaded by the ablated material. This significant effect would be of prime importance in nanofabrication and is currently under further investigation.

4. Conclusion

High porosity materials, such as the class of inorganic aerogels, offer a novel platform for dimensional reduction of microstructures and nanostructures, having the potential to advance beyond the currently available microstructure fabrication limits. The demonstrated approach is based on laser micro-ablation of surface relief and inner void micropatterns in silica aerogel monoliths, by using 193 nm ns and 800 nm fs laser pulses. Microstructures are subsequently densified by viscous sintering, leading to isotropic contraction of the monolith, together with the contraction of the microstructures embedded into the produced dense vitreous solid. Preliminary results provide evidence of an advantageous preferential densification of void structures at a ratio exceeding the nominally attained stereometric reduction, thus revealing a unique potential in nanofabrication. The presented approach can be extended to various aerogel material compositions, as well as to porous materials of different, organic or hybrid, nature, in order to provide novel solutions in the sectors of photonics, electronics, micromechanics, micro-fluidics, lab-on-chip chemical and environmental analysis, biomedicine and the like. This is an emerging concept holding a rather generic capacity, which can be further combined with a variety of established or new object forming techniques to open up novel routes for the future nanoscale technologies.

Acknowledgments

N.A.V. is grateful for his support in the frame of a Diamond Jubilee International Visiting Fellowship of the University of Southampton. Financial support via the EPSRC Ultrafast Laser Platform Grant No EP/J008052/1 at the ORC is gratefully acknowledged. N.A.V. also acknowledges the support of COST Action MP1205. The authors are grateful to I. Michaloudis, Th. Ioannidis and N. Leventis for the offer of a range of silica aerogel samples and the useful discussions. Many thanks go to I. Koutselas, D. Alexandropoulos, G. Avgouropoulos, M. Vasileiadis, Th. Mpatzaka, M. Feinäugle and D. J. Heath for their invaluable contributions. All data supporting this study are openly available from the University of Southampton repository at http://dx.doi.org/10.5258/SOTON/400836.